Finite Element inversion of DInSAR data from the Mw 6.3 L'Aquila Earthquake, 2009 (Italy)

E. Trasatti, C. Kyriakopoulos & M. Chini

(elisa.trasatti@ingv.it, christodoulos.kyriakopoulos@ingv.it, marco.chini@ingv.it)

Istituto Nazionale di Geofisica e Vulcanologia

Centro Nazionale Terremoti

Via di Vigna Murata 605

00143 Rome, Italy

Abstract

Fault slip distribution is usually retrieved from geodetic data assuming that the local crust is an elastic, homogeneous and isotropic half-space. In the last decades spatially dense geodetic data (e.g. DInSAR maps) have highlighted complex patterns of coseismic deformation that require new modeling tools, such as numerical methods, able to represent rheological and geometrical complexities of the Earth's crust. In this work, we develop a procedure to perform inversion of geodetic data based on the Finite Element method, accounting for a more realistic description of the local crust. The method is applied to the 2009 L'Aquila earthquake (M_w 6.3), using DInSAR images of the coseismic displacement. Results highlight the non-negligible influence of the medium structure: homogeneous and heterogeneous models show discrepancies up to 20% in the fault slip distribution values. Furthermore, in the heterogeneous models a new area of slip appears above the hypocenter. We also perform a resolution study, showing that the information about fault slip distributions retrieved from geodetic data should be considered as averaged on surrounding patches.

1. Introduction

On April 6th 2009, at 3:32 local time (1:32 UTC), a M_w 6.3 earthquake occurred in the Abruzzi region (central Italy), followed by five M > 5 aftershocks, the largest ones occurring on April 7th (M_w = 5.5) and 9th (M_w = 5.4) (Figure 1a). The mainshock, located at about 9 km depth, produced severe damage in the ancient city of L'Aquila and in many neighboring villages. Moment tensor solutions reveal normal faulting mechanism consistent with the NE-SW extensional trend of the central Apennines [e.g., Amato et al., 1998]. According to recent geodetic studies, surface geological observations and aftershocks relocations [Atzori et al., 2009; EMERGEO Working Group, 2010; Chiarabba et al., 2009], the main fault is identified as the NW striking and SW dipping Paganica Fault.

Inversions of geodetic data for seismic source purposes are often performed implementing the analytical model of Okada [1992] of a fault embedded in an elastic, homogeneous and isotropic half-space. It is reasonable to ask: how can material complexities affect slip distribution providing different surface displacement patterns? Analytical and semi-analytical codes such as Wang et al., [2003] provide a partial answer to this question, since they allow describing the lithosphere with a 1D vertical layering. However, local asperities, anisotropy and the presence of topography are likely to be present in faulted zones. The above mentioned complexities can be managed only by means of numerical tools. Masterlark [2003] tested the sensitivity of Finite Element (FE) computed slip distributions to common assumptions (e.g., homogeneous, isotropic, Poisson-solid and half-space medium), finding that differences in displacement predictions exceeded the uncertainty bounds. Hearn and Bürgmann, [2005] investigated the effect of depth-dependent elasticity on slip inversions using FE solutions of a shear dislocation in layered and uniform elastic Earth models. They found that incorporating realistic increases of shear modulus with depth in the inversions modifies the recovered centroid depth and seismic potency with respect to uniform elastic half-space models. Dubois et al., [2008] analyzed the influence of structural and rheological heterogeneities on the earthquake deformation cycle, showing significant differences in slip distribution (beyond the associated uncertainty bounds) when using models with fault damage zones and elastic layering.

In this paper, taking advantage of the FE method, we optimize the coseismic displacement data due to the L'Aquila earthquake to retrieve fault slip distributions. We also perform a resolution study to quantify the information we can extract from large coverage DInSAR data.

2. Data

Differential SAR Interferometry (DInSAR), a technique commonly used to measure coseismic ground displacements, provides spatially dense deformation fields with great accuracy [e.g., Chini et al., 2010]. The data used in this work are from the COSMO-SkyMed and ENVISAT satellite missions and their characteristics are summarized in Table 1. Phase noise is mitigated by an adaptive filter [Goldstein and Werner, 1998], while unwrapped interferograms are obtained by a Region Growing algorithm [Reigber and Moreira, 1997]. The topographic contribution is removed by a 5 meter resolution Digital Elevation Model (DEM). The three resulting interferograms (Figure 1), generated with a pixel spacing of 80 m, measure a congruent deformation pattern [Stramondo et al., 2011]. The maximum displacement is located between the city of L'Aquila and the town of Fossa, reaching respectively -16 cm (COSMO-SkyMed), -24 cm (ENVISAT ascending) and -27 cm (ENVISAT descending) in the SAR Line of Sight. Variations are due to the different look angles and orbits. In addition to DInSAR data, we consider GPS horizontal and vertical measurements of 8 sites within about 30 km from the epicenter [Anzidei et al., 2009], from continuous stations (Figure 1a, AQUI, INFN, INGP, SMCO) and from GPS receivers installed a few days before the main event (CADO, ROIO, SELL, CPAG).

The large amount of seismic data acquired during the L'Aquila sequence was subsequently used to investigate the characteristics of the local lithosphere. Di Stefano et al., [submitted to *Geophys. Res. Lett.*] performed a 3D tomography study using 1276 aftershocks until the end of June 2009. The images reveal vertical and lateral *vp* heterogeneities. The main feature is a high *vp* volume placed below the city of L'Aquila between 4-10 km depth. Furthermore, a receiver function study by Bianchi et al., [2010] shows lateral *vs* heterogeneities along the fault in the uppermost crust. The analysis of the AQU receiver function, the largest peak ground motion station [Cirella et al., 2009], highlights a high *vs* body (values up to 4.2 km/s) of 4-6 km thickness. This high velocity body, absent in the SE portion of the fault, may have influenced the kinematics of the L'Aquila seismic source.

3. FE models of the seismic source

We initially constrain the fault geometry using 5955 subsampled DInSAR data and 8 GPS data. We adopt the Okada [1992] fault as forward model to solve the non-linear optimization problem. The fault inversion is performed by a two-step algorithm consisting in a global search (Neighbourhood Algorithm) followed by a Bayesian inference on the generated ensemble of models [Sambridge 1999a,b]. This procedure extracts the most probable set of solutions, instead of a single best-fit model. The method has been largely tested for inversions of geodetic data in volcanic areas [Trasatti et al., 2008]. We perform tests aimed to find a reasonable balance between DInSAR and GPS points in the computation of the total misfit function, which is composed by the weighted sum of the reduced chi-square of each dataset (the three interferometric images are considered as a unique dataset). The relative weight of each dataset is fixed at 95% DInSAR and 5% GPS (see auxiliary material, Figure S1). The choice of the weights is due to the low uncertainty of the GPS data (few mm) which 'attracts' the misfit function towards a lowering of the GPS chi-square. The best-fitting fault parameters resulting from the optimization are reported in Table 2. All the parameters are well defined since they show peaked bell-like Posterior Probability Density (PPD) curves (Figures S2 and S3 for 1D and 2D PPD distributions, respectively). The resulting fault plane dimension and position are compatible, within their uncertainties, with previous findings [e.g. Atzori et al., 2009]. Regarding the fault orientation of our best model, the strike value of 142°±2° follows the line of converging DInSAR fringes (strike between 140° and 145°), emphasizing the primary role of large coverage data for fault geometry determination. The fault trace is compatible with the Paganica Fault surface trace as well (see Fig. 1a). The retrieved mean dip value is 42°±2, within the acceptable range of 40°-50°, typical for the NE trending structures of the Central Apennines [Amato et al., 1998].

In the following, we build FE models with the fault geometry determined above. Even if the fault plane is not fully optimized in the FE models, it is reasonable to suppose that potential variations of dip and strike values are within their previously determined uncertainty. Once the fault plane is constrained, our inverse problem is linear, provided we use linear elasticity. We set up a method consisting of three steps: *i)* building FE models of a fault embedded in a 3D domain, including topography and other characteristics; the fault is mapped by small patches; *ii)* computing a matrix of elementary 'Green's functions' for every slip patch; *iii)* performing linear inversions of the FE-computed matrix to retrieve the slip distribution. The FE models are composed of about 100'000 3D-brick elements contained in a cylindrical domain having radius of 100 km and height of 80 km. The fault plane dimensions in Table 2 are expanded up to 20 km in length and 15 km in width in order to map the slip distribution without edge artifacts, and subdivided into 300 1x1 km patches. The FE models also include the elastic structure, computed from the *vp* and *vs* anomalies resulting from the tomography by Di Stefano et al., [submitted]. We use a density profile of 2600 kg/m^3 above 4 km depth and 2800 kg/m^3 below it [Di Luzio et al., 2009]. The resulting Lame constants assume values such as μ = 18 GPa and λ = 30 GPa at shallow depths (1-3 km) and μ = 30 GPa and λ = 50 GPa below 10-14 km depth. The asperity found below the L'Aquila city at 4-10 km depth [Di Stefano et al., submitted; Bianchi et al., 2010] is reproduced by our FE model and is characterized by very high elastic parameters: μ = 40 GPa and λ = 54 GPa. The models include the topography of the area, generated using a DEM with pixels of 90 m. Four different models are considered: HOF, HOmogeneous with Flat topography medium, HEF, HEterogeneous with Flat topography, HOT, HOmogeneous with Topography and HET, HEterogeneous with Topography. For each model we perform the steps outlined above. We compute four 'Green's function' matrices, by collecting all the surface displacements for each model considered. The linear inversion is performed adopting the Occam's smoothing scheme [deGroot-Hedlin and Constable, 1990], minimizing the chi-square and the second order derivative (Laplacian) to avoid large oscillations in slip values. Positivity constraints are placed on slip to elude thrust components during the inversion, in contrast with the normal mechanism of the fault.

Slip distribution results are shown in Figure 2. The misfit lowers from 6.2, in case of the non-linear inversion, to 4.2 (HEF), 4.3 (HET) and 4.7 (HOF, HOT). Smoothing curves are shown in the auxiliary material, Figure S4. Results for all the models show that there is a large slip area in the central-SE part of the fault. The effect of topography can be appreciated by comparing results from HOF and HOT models, but differences are of second order. The small effect on the slip distribution could be related to the small topographic variations. Indeed, in areas with a strong topography, the effects on the slip distribution are larger [e.g, Kyriakopoulos et al., 2010]. More interesting features appear in the presence of an elastic structure. In the heterogeneous model HEF, the slip is distributed along the strike direction and it is concentrated between 3 and 7 km depth. A new local maximum of slip appears above the hypocenter, according to seismological inversions [Cirella et al., 2009]. The presence of the slip concentration above the hypocenter may be attributed to the presence of the high rigidity body, absent in the homogeneous models. The rake varies in the range -90°±4° in the high slipping areas. In the HET model the topography partially masks out the effect of the elastic structure, so that the resulting new high slip area due to the internal heterogeneities is more visible in the HEF model that in the HET model. The maximum slip is about 120 cm in the homogeneous models and 110 cm in the heterogeneous models. To better appreciate the changes introduced by the 3D elastic structure, Figure 2c,f show the differences between HEF and HOF, and between HET and HOT, respectively, reaching up to 20% of the maximum slip in both cases. The fault's hanging wall area shows low residual values (from 0 to 2.5 cm) for all three DInSAR images (Figure S5). In the foot wall area there are positive residuals for ENVISAT descending data and negative residuals for ENVISAT ascending data, reaching an absolute value of 5 cm in both cases.

An uncertainty analysis is performed to assess the reliability of our results. We compute the data covariance matrix **covd** and calculate the model covariance matrix **covm** [Menke, 1989]. The diagonal terms of **covm** are the variances of the slip values. Figure 3a shows the standard deviation associated with the slip distribution. Single slip values are acceptable since their uncertainty amounts to 2-4 cm for most part of the fault, degrading at fault bottom and borders. Following the approach outlined by Funning et al., [2005], we define a linear dimension of model resolution in order to assess the degree to which single slip values are averaged with the surroundings. In Figure 3b we observe that the resolving power rapidly decreases with depth. At hypocentral depths, the model resolves slip features larger than about 6 km. Thus, we must be aware that only general features of slip predictions based on geodetic data (even large coverage DInSAR data) should be considered, according to the intrinsic data resolving power and smoothing artifacts.

As a final remark, we perform inversions of new HOT and HET models with a steeper fault characterized by dip equal to 50°, based on recent seismological studies [e.g., Di Stefano et al., submitted]. Results are in general agreement with those previously obtained (Figure S6).

4. Discussion and conclusions

All the slip distributions show a wide slip area located in the central-SE part of the fault, in agreement with previous results [Atzori et al., 2009, Cirella et al., 2009]. However, Cirella et al., [2009] retrieved a slip distribution deeper than the hypocenter, making use of seismological data. This result cannot be obtained from geodetic data. Indeed, in Figure 3 we show that even dense DInSAR data are unsuitable to resolve deep slip features. We also show that using heterogeneous models such as HEF and HET, the maximum slip area is flattered and shifted NW, and a new patch of slip appears above the hypocenter. This feature doesn't appear in geodetic inversions with Okada [1992] models [e.g., Atzori et al., 2009] but it is common only to inversions in non-homogeneous models [e.g., Cirella et al., 2009]. We can compare the results for the slip distributions with the elastic characteristics close to the fault plane (Figure 4). In the HEF model, the slip is concentrated between 5-10 km depth, and distributed along the strike direction. This could be due to the low shear modulus of the shallow layers, which amplifies the deformation in extension and absolute value. However, the inversion algorithm, trying to fit the observed data, produces an opposite behavior. Indeed, in the heterogeneous models the slip distribution is more concentrated, we get a lower maximum slip and a new slip area appears in correspondence of the high rigidity body below L'Aquila city. The most important result of our inversions is that the 3D elastic structure introduces differences in the slip distribution that are not negligible. We obtain differences up to 20%. Topography does not have a critical influence on slip distribution since the main differences are due to the presence of elastic heterogeneities.

The resulting scalar moments are $M_0 = 2.5 \times 10^{18}$ Nm for HOF and HOT, using an average shear modulus value of 30 GPa, corresponding to $M_w = 6.2$, and $M_0 = 1.2 \times 10^{18}$ Nm for HEF and HET, corresponding to $M_w = 6.0$. The value in the heterogeneous models is lower than the observed $M_w = 6.3$ because of the low shear modulus values near the fault at shallow depths. While the 'Green's function' feels the effect of the whole elastic structure, as described above, the moment density is proportional to the local shear modulus and slip. Therefore, the scalar moment computed in the heterogeneous models is lower than the homogeneous ones because of the combined effect of the slip concentration and of the low shear modulus values at shallow depths.

Dense and large coverage DInSAR data is very useful to determine the fault geometry, but we must keep in mind that geodetic data, even DInSAR data, is characterized by poor resolution at large depths. Furthermore, the information about fault slip distribution should be considered as averaged on surrounding patches, even in complex models such as those shown.

Acknowledgments

Many thanks to the LabTel group from INGV-Rome for the scientific and technical support. We thank M. Bonafede and R. Di Stefano for helpful discussions. C. Chiarabba and P. De Gori are acknowledged for providing tomographic data. Two anonymous reviewers improved the quality of the manuscript. J. P. Merryman Boncori improved the English of the manuscript. This work is partially funded by the Italian Space Agency (ASI) through the SiGRiS project.

References

Amato, A., et al. (1998), The 1997 Umbria-Marche, Italy, Earthquake Sequence: A first look at the main shocks and aftershocks, *Geophys. Res. Lett.*, *25*, 2861-2864.

Anzidei, M., et al. (2009), Coseismic deformation of the destructive April 6, 2009 L'Aquila earthquake (central Italy) from GPS data, *Geophys. Res. Lett.*, *36*, L17307.

Atzori, S., I. Hunstad, M. Chini, S. Salvi, C. Tolomei, C. Bignami, S. Stramondo, E. Trasatti, A. Antonioli, and E. Boschi (2009), Finite fault inversion of DInSAR coseismic displacement of the 2009 L'Aquila earthquake (Central Italy), *Geophys. Res. Lett.*, *36*, L15305.

Bianchi, I., C. Chiarabba, and N. Piana Agostinetti (2010), Control of the 2009 L'Aquila earthquake, central Italy, by a high velocity structure: a Receiver Function study, *J. Geophys. Res., 115*, B12326.

Chiarabba, C., et al. (2009), The 2009 L'Aquila (central Italy) M_w 6.3 earthquake: Main shock and aftershocks, *Geophys. Res. Lett.*, *36*, L18308.

Chini, M., S. Atzori, E. Trasatti, C. Bignami, C. Kyriakopoulos, C. Tolomei, and S. Stramondo (2010), The May 12, 2008, (Mw 7.9) Sichuan Earthquake (China): Multi-frame ALOS – PALSAR DInSAR Analysis of Coseismic Deformation, *IEEE Geosci. Rem. Sens. Lett.*, *7*, 266-270.

Cirella, A., A. Piatanesi, M. Cocco, E. Tinti, L. Scognamiglio, A. Michelini, A. Lomax, and E. Boschi (2009), Rupture history of the 2009 L'Aquila (Italy) earthquake from non-linear joint inversion of strong motion and GPS data, *Geophys. Res. Lett.*, *36*, L19304.

deGroot-Hedlin, C. and S. Constable (1990), Occam's inversion to generate smooth, two-dimensional models from magnetotelluric data, *Geophysics, 55*, doi:10.1190/1.1442813.

Di Luzio, E., et al. (2009), Moho deepening and shallow upper crustal delamination beneath the central Apennines, *Earth Plan. Sci. Lett., 280*, 1-12.

Dubois, L., K. Feigl, D. Komatisch, T. Arnadottir and F. Sigmundsson (2008), Three-dimensional mechanical models for the June 2000 earthquake sequence in the south Iceland seismic zone, *Tectonophys., 475,* 12-29.

EMERGEO Working Group (2010), Evidence for surface rupture associated with the M_w 6.3 L'Aquila earthquake sequence of April 2009 (central Italy), *Terra Nova*, *22*, 43–51.

Funning, G. J., B. Parsons, T. J. Wright, J. A. Jackson, and E. J. Fielding (2005), Surface displacements and source parameters of the 2003 Bam (Iran) earthquake from ENVISAT advanced synthetic aperture radar imagery, *J. Geophys. Res.*, *110*, B09406.

Goldstein, R. M., and C. L. Werner (1998), Radar interferogram filtering for geophysical applications, *Geophys. Res. Lett.*, *25*, 4035 – 4038.

Hearn, E.H., and Bürgmann, R. (2005), The effect of elastic layering on inversions of GPS data for coseismic slip and resulting stress changes: strike-slip earthquakes, *Bull. Seism. Soc. Am., 95,* doi: 10.1785/0120040158.

Kyriakopoulos, C., E. Trasatti, S. Atzori, C. Bignami, M. Chini, S. Stramondo, and C. Tolomei (2010), The M_w 7.9 Wenchuan (China) Earthquake: exploring the role of crustal heterogeneities from finite element analysis of DInSAR coseismic deformation, *Geophys. Res. Abstr., 12*, EGU2010-9315.

Masterlark, T. (2003), Finite element model predictions of static deformation from dislocation sources in a subduction zone: sensitivities to homogeneous, isotropic, Poisson-solid, and half-space assumptions, *J. Geophys. Res.*, *108*, doi:10.1029/2002JB002296.

Menke, W. (1989), Geophysical Data Analysis: Discrete Inverse Theory, Rev. Ed, Academic Press San Diego, 289 pp.

Okada, Y. (1992), Internal deformation due to shear and tensile faults in a half-space, *Bull. Seismol. Soc. Am.*, *82*, 1018-1040.

Reigber, A., and J. Moreira (1997), Phase unwrapping by fusion of local and global methods, *Proc. IEEE Geosci. Rem. Sens. Symp., 2*, 869–871.

Sambridge, M. (1999), Geophysical inversion with a neighbourhood algorithm - I. Searching a parameter space, *Geophys. J. Int.*, *138*, 479-494.

Sambridge, M. (1999), Geophysical inversion with a neighbourhood algorithm - I. Searching a parameter space, *Geophys. J. Int.*, *138*, 727-746.

Stramondo, S., M. Chini, C. Bignami, S. Salvi, and S. Atzori (2011), X-, C-, and L-band DInSAR investigation of the April 6, 2009, Abruzzi earthquake, *IEEE Geosci. Rem. Sens. Lett.*, 8, 49-53.

Trasatti, E., C. Giunchi, and N. P. Agostinetti (2008), Numerical inversion of deformation caused by pressure sources: application to Mount Etna (Italy), *Geophys. J. Int.*, *172*, 873-884.

Wang, R., F.L. Martin, and F. Roth (2003), Computation of deformation induced by earthquakes in a multi-layered elastic crust - FORTRAN programs EDGRN/EDCMP, *Comput. Geosci., 29*, 195-207.

Figure captions

Figure 1. a) Map of the L'Aquila region. The focal mechanisms of the mainshock and the larger aftershocks are in accordance with the NW-SE extensional trend of the central Apennines. The aftershock sequence until the end of April 2009 is shown in blue and GPS stations are drawn with black triangles. The surface trace of the Paganica Fault is shown in red and the fault retrieved by non-linear inversion is drawn with white dashed line. b) COSMO-Skymed wrapped phase (ascending orbit) of the coseismic displacement. c) ENVISAT ascending wrapped phase. d) ENVISAT descending wrapped phase. Coordinates are in UTM-WGS84 projection, zone 33.

Figure 2. Slip distributions retrieved by linear inversions. a) HOF model; b) HEF model; c) difference between HEF and HOF; d) HOT model; e) HET model; f) difference between HET and HOT. Models: HOF, homogeneous and flat; HEF, heterogeneous and flat; HOT, homogeneous with topography; HET, heterogeneous with topography. The grey arrows represent the rake. The star indicates the hypocenter.

Figure 3. a) Standard deviation associated with the slip distribution for the HET model. Similar results are obtained with the other models. b) Resolution study. The linear resolution parameter represents the dimension at which patch features may be resolved.

Figure 4. a) Fault slip distribution within the FE HET model; b) elastic properties (shear modulus) next to the fault plane, as implemented in the model.

Tables

Table 1. Characteristics of the interferograms used.

Mission	Orbit	Acquisition Date	Perpendicular Baseline (m)	Incidence angle (°)	Fringe Rate (cm)
COSMO-SkyMed	Ascending	04/04/2009 12/04/2009	435	38	3.1
ENVISAT	Ascending	11/03/2009 15/04/2009	237	23	5.6
ENVISAT	Descending	27/04/2008 12/04/2009	41	23	5.6

Table 2. Fault parameters retrieved by non-linear inversion.

Easting [a,b] (km)	Northing [a,b] (km)	Depth [b] (km)	Length (km)	Width (km)	Strike (°)	Dip (°)	Slip (cm)	Rake (°)
368.9±0.7 [c]	4693.9±0.7 [c]	-2.3±0.7 [c]	12.5±0.5 [c]	10.8±0.8 [c]	142±2 [c]	42±2 [c]	53±5 [c]	-96±4 [c]

[a] Easting and Northing coordinates are in UTM-WGS84 projection, zone 33.

[b] The fault position (Easting, Northing, depth) is referred to the top left corner.

[c] The standard deviation of every parameter is estimated from the half-width of the PPD distributions (auxiliary material Figure S2).

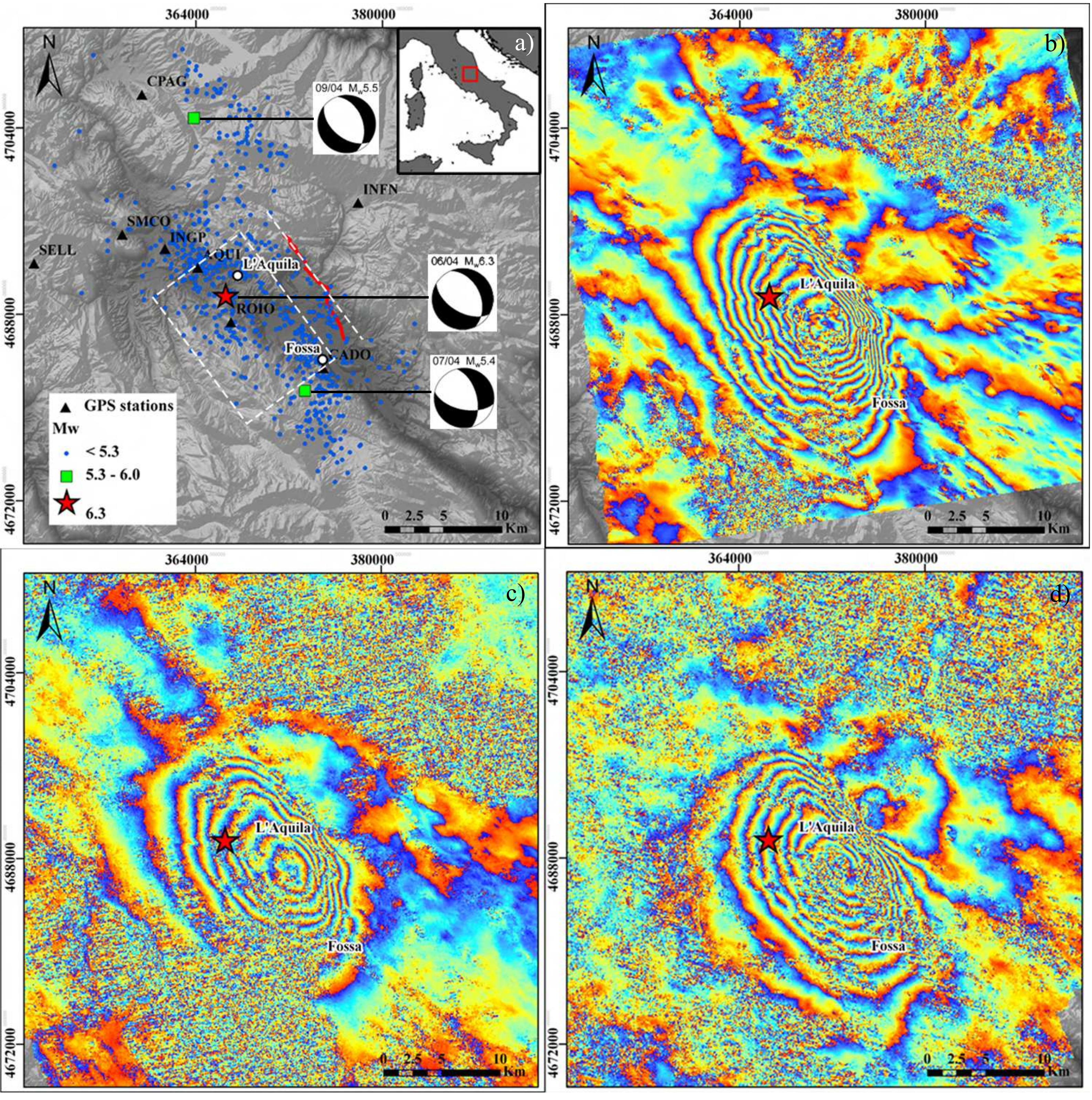

a)
b)
c)
d)
N
364000
380000
4704000
4688000
4672000
CPAG
SMCO
SELL
INGP
AQUI
INFN
ROIO
CADO
L'Aquila
Fossa
09/04 Mw5.5
06/04 Mw6.3
07/04 Mw5.4
GPS stations
Mw
< 5.3
5.3 - 6.0
6.3
0 2.5 5 10
Km

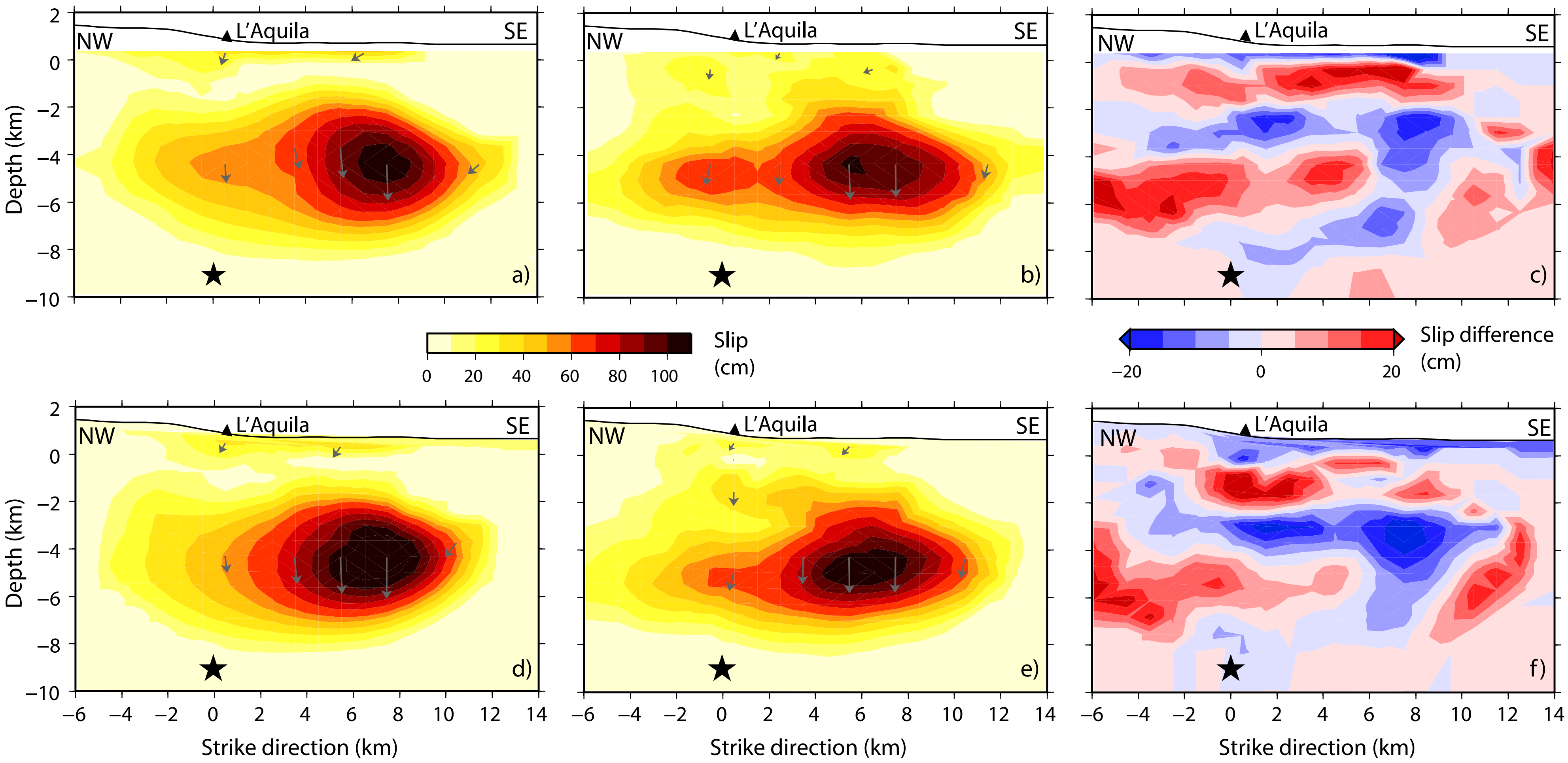

a)
b)
c)
d)
e)
f)
NW
SE
L'Aquila
Depth (km)
Strike direction (km)
Slip
(cm)
Slip difference
(cm)

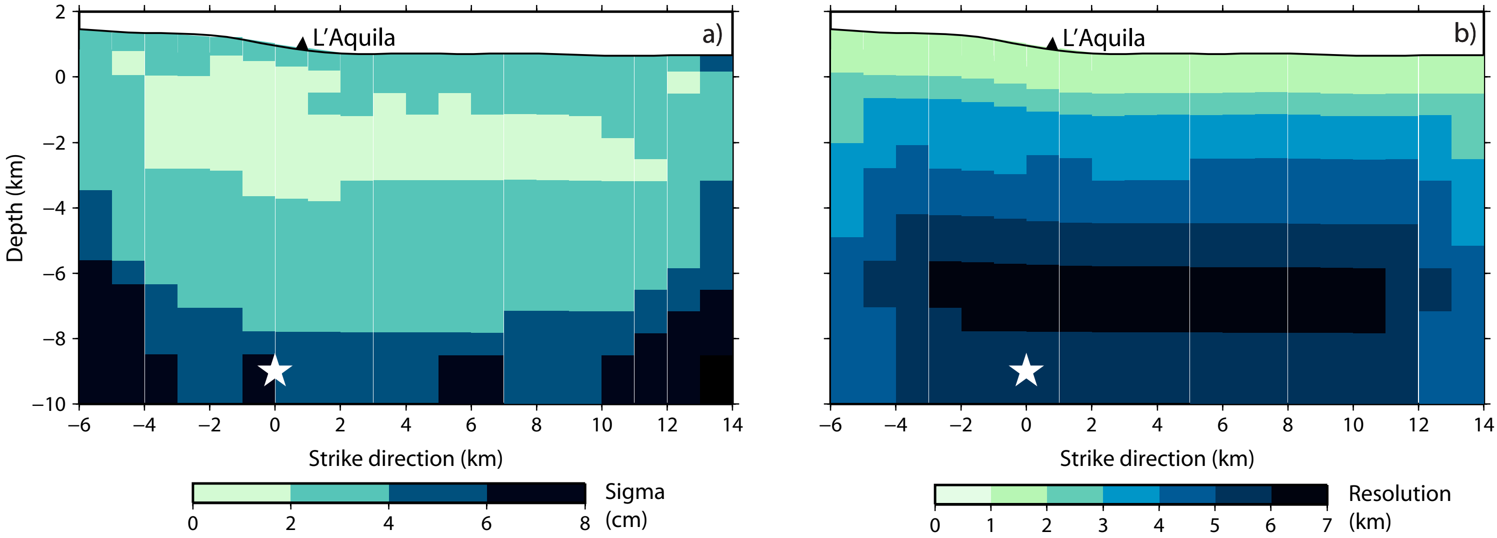

a)
L'Aquila
Depth (km)
Strike direction (km)
Sigma
(cm)
b)
L'Aquila
Strike direction (km)
Resolution
(km)

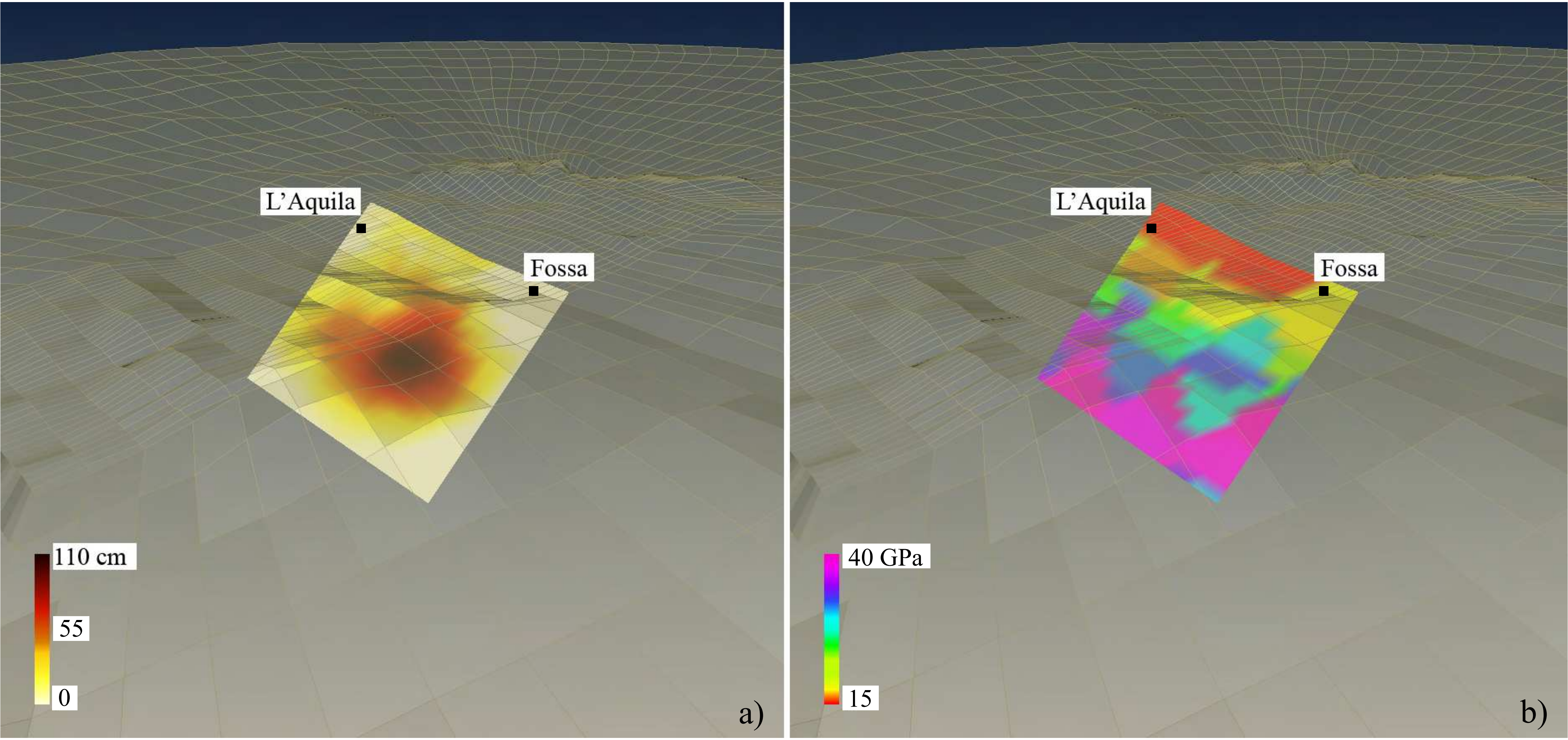
L'Aquila
Fossa
110 cm
55
0
a)
L'Aquila
Fossa
40 GPa
15
b)